The Astrophysical Journal, 865:50 (15pp), 2018 September 20 https://doi.org/10.3847/1538-4357/aadb9b

Modeling the Thermodynamic Evolution of Coronal Mass Ejections Using Their Kinematics

Wageesh Mishra and Yuming Wang
CAS Key Laboratory of Geospace Environment, Department of Geophysics and Planetary Sciences, University of Science and Technology of China, Hefei 230026, People's Republic of China; wageesh@ustc.edu.cn, ymwang@ustc.edu.cn
Received 2018 June 9; revised 2018 August 9; accepted 2018 August 17; published 2018 September 20

Abstract

Earlier studies on coronal mass ejections (CMEs), using remote sensing and in situ observations, have attempted to determine some internal properties of CMEs, which were limited to a certain position or a certain time. To understand the evolution of the internal thermodynamic state of CMEs during their heliospheric propagation, we improve the self-similar flux-rope internal state model, which is constrained by the measured propagation and expansion speed profiles of a CME. We implement the model in a CME that erupted on 2008 December 12 and probe the internal state of the CME. It is found that the polytropic index of the CME plasma decreased continuously from 1.8 to 1.35 as the CME moved away from the Sun, implying that the CME released heat before it reached an adiabatic state and then absorbed heat. We further estimate the entropy changing and heating rate of the CME. We also find that the thermal force inside the CME is the internal driver of CME expansion while the Lorentz force prevented the CME from expanding. It is noted that the centrifugal force due to poloidal motion decreased at the fastest rate, and the Lorentz force decreased slightly faster than the thermal pressure force as the CME moved away from the Sun. We also discuss the limitations of the model and approximations made in the study.

Key words: Sun: coronal mass ejections (CMEs) – Sun: heliosphere

1. Introduction

Coronal mass ejections (CMEs) are large-scale structures containing mass, kinetic energy, and magnetic flux that are expelled from the Sun into the heliosphere (Tousey 1973; Hundhausen et al. 1984; Chen 2011; Webb & Howard 2012). The CMEs in the heliosphere are referred to as interplanetary coronal mass ejections (ICMEs), which are often understood to be flux ropes maintaining their magnetic connection to the Sun while propagating in the solar wind (Larson et al. 1997). They are of interest to the scientific community because by studying them, we can enhance our understanding of the (i) physical process responsible for the removal of built-up magnetic energy and plasma from the solar corona, (ii) kinematic and thermodynamic evolution of an expanding magnetized plasma blob in an ambient magnetofluid medium, and (iii) mechanism for exchange of energy and plasma dynamics between different plasma regions (Lopez et al. 2000; Low 2001; Howard et al. 2007). They are also of interest to the technical community because they are the main drivers of severe space weather that lead to the disruption of a range of technologies such as communications systems, electronic circuits, and power grids on Earth, and thus our technology is vulnerable to them (Schwenn 2006; Pulkkinen 2007; Baker 2009).

CMEs have been detected by remote sensing and in situ spacecraft observations for decades. Until a decade ago, CMEs were routinely imaged only near the Sun primarily by coronagraphs on board spacecraft. The launch of the *Solar TErrestrial RElations Observatory* (*STEREO*) in 2006 (Kaiser et al. 2008) provided us with the opportunity to track CMEs continuously between the Sun and Earth from multiple viewpoints (Lugaz et al. 2009; Liu et al. 2010b; Davies et al. 2012; Rollett et al. 2016). Most of the studies have focused on the signatures of origins for CMEs, their dynamic evolutions, masses, arrival times, induced radio bursts, geo-effectiveness, and connection between magnetic flux ropes measured in situ and CME structures observed by coronagraphs and heliospheric imagers (Munro et al. 1979; Webb et al. 2000; Cliver & Hudson 2002; Wang et al. 2002; Schwenn et al. 2005; Forsyth et al. 2006; Gopalswamy et al. 2009; Kilpua et al. 2012; DeForest et al. 2013; Mishra & Srivastava 2015; Mishra et al. 2017; Shen et al. 2017; Harrison et al. 2018). There have been a few studies exploiting the radio, X-ray, and EUV imaging as well as in situ observations for understanding the thermodynamic properties of the CMEs.

EUV spectral observations from the ultraviolet coronagraph spectrometers (UVCS), coronal Diagnostic Spectrometer, and solar ultraviolet measurements of emitted radiation instruments on the *SOlar and Heliospheric Observatory* (*SOHO*; Domingo et al. 1995) have helped us to infer the density, temperature, ionization state, and Doppler velocity of CMEs (Raymond 2002; Kohl et al. 2006; Lee et al. 2009). They have also suggested that CMEs are loop-like structures with a helical magnetic field and probably have higher temperature than the inner corona (Antonucci et al. 1997; Ciaravella et al. 2000). The heating rates of CMEs inferred from UVCS observations show that heating of the CME material continues out to $3.5\,R_{\odot}$ and is comparable to the kinetic and gravitational potential energies gained by the CMEs (Akmal et al. 2001; Ciaravella et al. 2003). Recently, Bemporad & Mancuso (2010) estimated the physical parameters of plasma (temperature and magnetic field) in the pre- and post-shock regions using white-light, EUV, and radio observations of a fast CME. The combination of the density, temperature, and ionization stated of CMEs constrains their thermal history and has been used to understand the physical processes within CME plasma.

Some internal properties of CMEs have also been measured near and beyond 1 au from their in situ observations by instruments on board the *Voyager, Ulysses, Helios, Wind, ACE*, and *STEREO* spacecraft. For example, CMEs in in situ observations show the structure of a spiral magnetic field,

low plasma beta, and low temperature compared to those in the ambient solar wind (Burlaga et al. 1981; Richardson & Cane 1993). The reason for the lower temperature is the expansion of CMEs during their propagation as their leading edges usually move faster than the trailing edges and/or pressures inside CMEs are higher than those in the ambient solar wind. Measuring the properties of an individual ICME through the heliosphere is not always possible due to the sparse distribution of in situ spacecraft, which are rarely radially aligned, and further, due to the difficulty in identifying ICMEs in the solar wind. The ion charge states in ICMEs are often higher, implying high temperature (several million Kelvin) at their solar source (Lepri et al. 2001; Zurbuchen et al. 2003). The thermodynamic evolution of ICMEs has been statistically studied using in situ observations taken over a range of radial distances from 0.3 to 30 au in the heliosphere (Wang & Richardson 2004; Liu et al. 2005, 2006; Wang et al. 2005). These studies have demonstrated the Coulomb collision within ICMEs (Liu et al. 2005, 2006) and their moderate expansion compared with theoretical predictions. They also showed that the magnetic field and temperature decrease faster in ICMEs than in the solar wind, but the temperature decreases more slowly in ICMEs than in the solar wind (Liu et al. 2006). This implied that the plasma in the ICMEs must be heated. The radial expansion speed of ICMEs is found to be of the order of the Alfvén speed (Jian et al. 2008). Global MHD modeling of ICMEs based on a polytropic approximation to the energy equation has also been done to interpret the observations (Riley et al. 2003; Manchester et al. 2004). However, the polytropic process and turbulence dissipation (Goldstein et al. 1995) are intrinsically different, and therefore, modeling the thermodynamic state of CMEs is difficult.

Although there are a few studies addressing the internal states of CMEs, most of them provide thermodynamics of CMEs only at a certain heliocentric distance and/or at a certain time. Based on statistical surveys using multispacecraft measurements, the polytropic index of CME plasmas was suggested to be around 1.1 to 1.3 from 0.3 to 20 au, which is about constant over a solar cycle (Liu et al. 2005, 2006), while the polytropic index for solar wind is noted to be 1.46 (Totten et al. 1995). Thus, the expansion of an ICME behaves more like an isothermal than an adiabatic process, which has a polytropic index of 1.66. However, the understanding of the continuous evolution of the internal state of an individual CME during its heliospheric propagation is still limited.

So far, the only attempt to figure out the internal state of an individual CME during its propagation in the outer corona has been done by Wang et al. (2009, hereafter Paper I), in which a model to reveal the Flux Rope Internal State (FRIS) was developed. Using the model, one could infer the internal forces and thermodynamic properties of CMEs from coronagraph and heliospheric imager observations. In their study, they estimated the polytropic index of CME plasma and suggested that there is continuous heat injection into the CME plasma. They also found that thermal pressure caused the CME expansion while the magnetic force prevented the CME from expanding, and both forces decreased continuously as the CME moved away from the Sun. However, there was a mistake in deriving Equation (10) in Paper I, and although it did not affect the final results of their work, the use of the polytropic equation of state (Equation (12) in Paper I) was not proper. Generally, a polytropic process is a thermodynamic process that obeys the relation between a fluid's thermal pressure (p) and density (ρ) by means of an index (Γ) described as

$$p = b\rho^{\Gamma}, \tag{1}$$

where both Γ and b are not constants and change with time. It describes the change of state of any fluid. We emphasize that the value of b was kept constant in Paper I, which was incorrect. This is because b should change when a thermodynamic system evolves from one polytropic process to another. Further, we use the equations of thermodynamics and derive a few additional parameters, such as absorbed heat, entropy, heating rate, and entropy changing rate of the CME. Thus, in the present study, we improve the FRIS model (Section 2) and apply it to the CME of 2008 December 12 to demonstrate what we can learn from the observations with the aid of the model (Section 3). A summary and discussion of our study are presented in Section 4.

2. Flux-rope Model for a CME's Internal State

In this model, a CME is treated as an axisymmetric cylinder with self-similar expansion. The self-similar assumption assumes that the distributions of the quantities along the radial direction in the flux-rope frame (with the z-axis in cylindrical coordinates along the flux-rope axis) remains unchanged during the propagation of the CMEs. Using this model, one could infer the internal forces and thermodynamic properties of CMEs from coronagraph observations. The derivation of the improved model is similar to that in Paper I except for some necessary corrections. For the completeness of this paper, we describe the details of the whole derivation below.

2.1. Derivation of the FRIS Model

We begin with the assumption that CMEs are an axisymmetric cylindrical flux rope in the local scale, even though in the global scale they may be a loop-like structure with two ends rooted on the surface of the Sun. Therefore, a flux rope can be treated axisymmetrically in the cylindrical coordinates (r, ϕ, z) with the origin on the axis of the flux rope (Figure 1), and we have $\frac{\partial}{\partial\phi} = \frac{\partial}{\partial z} = 0$. Since the cross-section of the flux rope is a circle, we assume its radius to be R, which is a time-dependent parameter. Considering the flux-rope geometry, the expansion speed of the flux rope's boundary is given by

$$v_e(t) = \frac{dR(t)}{dt}, \tag{2}$$

and the expansion acceleration at the boundary of the flux rope is

$$a_e(t) = \frac{dv_e(t)}{dt}. \tag{3}$$

Further, assuming that the flux rope is undergoing a self-similar expansion within the cross-section, we can get a dimensionless variable

$$x = \frac{r}{R}, \tag{4}$$

which is the normalized radial distance from the flux-rope axis and independent of time. $x = 1$ is the boundary of the flux rope. This expresses any self-similar variable as the product of a function of x and a function of t. Under this treatment, the radial (r) and azimuthal (ϕ) components of velocity can be

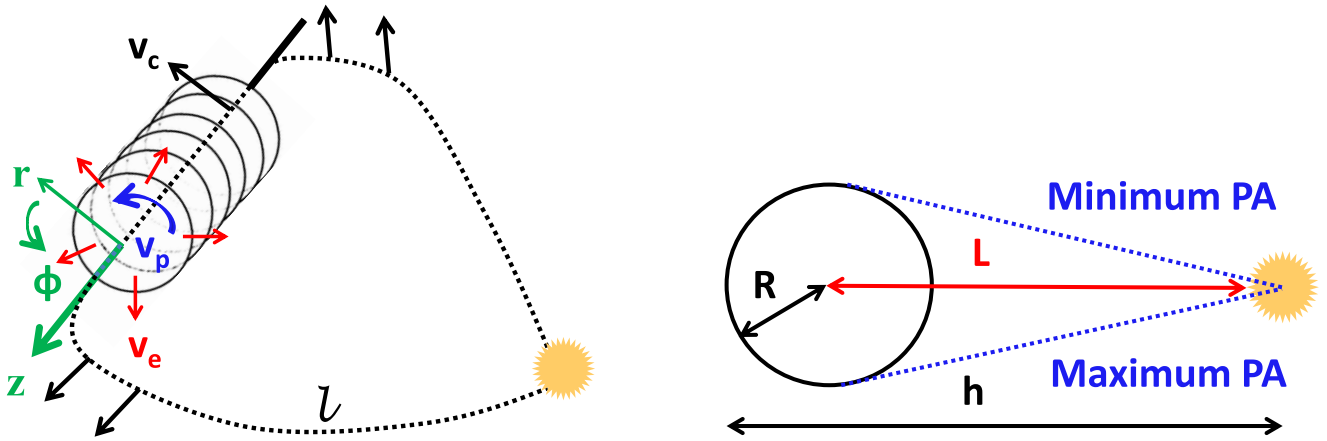

Figure 1. Left panel: schematic picture of a flux-rope CME. The black dashed line indicates the looped axis of the flux rope with the axial length l. A cylindrical coordinate system (i.e., r, ϕ, z) is attached to the the axis of the flux rope (in green). The three types of global motions of the flux-rope CME is represented. The linear propagation speed (v_c), expansion speed (v_e), and poloidal speed (v_p) are shown by the black, red, and blue arrows, respectively. v_c is the speed in a rest reference frame, while v_e and v_p are the speeds at the boundary of the flux rope in a plane perpendicular to the axis of the flux rope. Right panel: schematic picture for the cross-section of the CME flux rope. The radius of the flux rope is R, L is the distance from the flux-rope axis to the solar surface, h is the heliocentric distance of the CME leading edge, and the minimum and the maximum position angles are shown by the dotted blue lines (adapted from Wang et al. 2009).

expressed as

$$v_r(t, x) = \frac{d}{dt}(xR) = xv_e(t), \tag{5}$$

$$v_\phi(t, x) = f_{v_\phi}(x)v_p(t), \tag{6}$$

where v_p is the poloidal speed at the boundary of the flux rope. The poloidal speed of CME plasma is dependent on both the time and its location from the axis of the CME flux rope. Thus, the radial component of acceleration can be expressed as

$$a_r(t, x) = \frac{d\boldsymbol{v}(t, x)}{dt} \cdot \hat{\boldsymbol{r}} = xa_e(t) - \frac{v_\phi^2(t, x)}{xR}. \tag{7}$$

Thus, the first term on the right-hand side of Equation (7) is the acceleration of the radial motion of the plasma, and the second term is the acceleration contributed by the circular/poloidal motion of the plasma.

2.1.1. Conservations of Total Mass and Angular Momentum

Under the assumption of self-similar expansion and considering that magnetic field lines are frozen-in with the plasma flows, the density in the flux rope has a fixed distribution $f_\rho(x)$, and therefore, the density (ρ) in the flux rope can be expressed as

$$\rho(t, x) = f_\rho(x)\rho_0(t), \tag{8}$$

where ρ_0 is the average density of the flux rope. The conservation of total mass (M) is expressed as

$$M = \int \rho r dr d\phi dz = 2\pi l\rho_0 \int_0^R f_\rho(x) r dr$$

$$= 2\pi l R^2 \rho_0 \int_0^1 f_\rho(x) x dx, \tag{9}$$

where l is the axial length of the flux rope (Figure 1). The average density of the flux rope is

$$\rho_0(t) = \overline{\rho} = \frac{M}{\pi l R^2}. \tag{10}$$

Combining Equations (9) and (10), we get $\int_0^1 f_\rho(x) x dx = 1/2$. Further, the total angular momentum of the flux rope is expressed as

$$L_A = \int \rho r v_\phi r dr d\phi dz = 2\pi l R^3 \int_0^1 \rho v_\phi x^2 dx$$

$$= 2\pi l R^3 \rho_0(t) v_p(t) \int_0^1 f_\rho(x) f_{v\phi}(x) x^2 dx. \tag{11}$$

Combining Equations (10) and (11), we may derive

$$v_\phi(t, x) = \frac{k_1 L_A}{MR} f_{v\phi}(x), \tag{12}$$

where $k_1 = \frac{1}{2\int_0^1 f_\rho(x) f_{v\phi}(x) x^2 dx}$.

2.1.2. Equation of Motion

We investigate the motion of an arbitrary fluid element using momentum conservation equation (in the frame, frozen-in with the moving flux rope) as

$$\rho \frac{\partial \boldsymbol{v}}{\partial t} + \rho(\boldsymbol{v} \cdot \nabla)\boldsymbol{v} = -\nabla p + \boldsymbol{j} \times \boldsymbol{B}, \tag{13}$$

where p is the plasma thermal pressure, $\boldsymbol{B} = (0, B_\phi, B_z)$ is the magnetic induction, and $\boldsymbol{j} = \frac{1}{\mu_0}(\nabla \times \boldsymbol{B})$ is the current density. Here, the viscous stress tensor (S), gravity force ($\boldsymbol{F}_g$), and the equivalent fictitious force ($\boldsymbol{F}_a$) due to the use of a non-inertial reference frame opposite to the acceleration are ignored. The validity of this consideration is discussed in Section 4. Equation (13) can be decomposed into the $\hat{\boldsymbol{r}}$ and $\hat{\phi}$ components, and we have

$$\hat{\boldsymbol{r}}: \ \rho\frac{\partial v_r}{\partial t} + \rho\left(v_r\frac{\partial v_r}{\partial r} - \frac{v_\phi^2}{r}\right) = -\frac{\partial p}{\partial r} + (\boldsymbol{j} \times \boldsymbol{B})_r \tag{14}$$

$$\hat{\phi}: \ \frac{\partial v_\phi}{\partial t} + v_r\frac{\partial v_\phi}{\partial r} + \frac{v_r v_\phi}{r} = 0. \tag{15}$$

Equation (15) means that there is no force acting in the azimuthal ($\hat{\phi}$) direction, and the angular momentum is conserved. Substituting the v_r and v_ϕ in Equation (14) with those from Equations (5) and (12), respectively, we obtain

$$(\boldsymbol{j}\times\boldsymbol{B})_r = \rho\left(a_e x - \frac{k_1^2 L_A^2 f_{v\phi}^2}{M^2 x R^3}\right) + \frac{\partial p}{\partial r}. \tag{16}$$

2.1.3. Equations of Thermodynamics

The laws of thermodynamics (i.e., the relationships between heat, work, and the properties of the system in equilibrium) are expressed and fall within the constraints imposed by the thermodynamic equations. For ideal gases and reversible processes, the first and second laws of thermodynamics are expressed in the form of Equations (17) and (18) as

$$du = dQ - pd\frac{1}{\rho}, \tag{17}$$

$$ds = \frac{dQ}{T}, \tag{18}$$

where $u = \frac{p}{(\gamma-1)\rho}$, and $p = nk(T_p + T_e) = 2nkT$. In these formulations, p, u, Q, and s are the thermal pressure, internal energy per unit mass, heat per unit mass and entropy per unit mass, respectively. ρ is the mass density of protons, and n is the number density of protons, and thus, $n = \frac{\rho}{m_p}$, where m_p is the proton mass. γ is the adiabatic index, which is $5/3$ for monoatomic ideal gases. T_p and T_e are the temperatures of proton and electron, respectively, and $T = \frac{1}{2}(T_p + T_e)$ is the average temperature between the two species. Equation (18) can be rewritten by using the formulations noted above,

$$\begin{aligned} Tds &= du + pd\frac{1}{\rho} \\ &= \frac{p}{(\gamma-1)\rho} d\ln\left(\frac{p}{\rho^\gamma}\right) \end{aligned} \tag{19}$$

$$\begin{aligned} \Rightarrow \ln\left(\frac{p}{\rho^\gamma}\right) &= \frac{(\gamma-1)m_p}{2k}(s+s_0) \\ &= \frac{(\gamma-1)m_p}{2k} s, \quad [\text{WLOG using } s \text{ for } s+s_0] \\ \Rightarrow p &= e^{\frac{(\gamma-1)m_p}{2k}s}\rho^\gamma. \end{aligned} \tag{20}$$

Since $\sigma = \frac{(\gamma-1)m_p}{2k}$ is a constant, we can therefore write for our considered flux rope as

$$p(t, r) = e^{\sigma s}\rho^\gamma. \tag{21}$$

The polytropic process is described in Equation (1) and combining that with Equation (21), we obtain

$$e^{\sigma s} = b\rho^{\Gamma-\gamma}. \tag{22}$$

2.1.4. Lorentz Force and Helical Magnetic Field Structure

We calculate the average Lorentz force ($\overline{f}_{\rm em}$) by integrating Equation (16) over the cross-section of the flux rope and substituting in the p and ρ from Equations (21) and (8), respectively. Thus, we have

$$\begin{aligned} \overline{f}_{\rm em} &= \frac{2}{R^2}\int_0^R (\boldsymbol{j}\times\boldsymbol{B})_r r dr \\ &= \frac{k_2 M a_e}{lR^2} - \frac{k_1^2 k_3 L_A^2}{MlR^5} - \frac{k_4 M^\gamma e^{\sigma s}}{l^\gamma R^{\gamma+1}}, \end{aligned} \tag{23}$$

where $k_2 = \frac{2}{\pi}\int_0^1 f_\rho x^2 dx > 0$, $k_3 = \frac{2}{\pi}\int_0^1 f_\rho f_{v\phi}^2 dx \geqslant 0$, and $k_4 = \frac{2}{\pi^\gamma}\left[\int_0^1 f_\rho^\gamma dx - f_\rho^\gamma(1)\right]$ are integral constants. The first two terms on the right-hand side of Equation (23) are the average total force due to the expansion and poloidal motion, and the third term is the average thermal pressure force,

$$\overline{f}_{\rm th} = \frac{k_4 M^\gamma e^{\sigma s}}{l^\gamma R^{\gamma+1}}. \tag{24}$$

Further, the magnetic field in an axisymmetric cylindrical flux rope can be written as

$$\begin{aligned} &\boldsymbol{B} = B_\phi\hat{\phi} + B_z\hat{z} = \nabla\times\boldsymbol{A} \\ &B_\phi = -\frac{\partial A_z}{\partial r} \quad \text{and} \quad B_z = \frac{1}{r}\frac{\partial}{\partial r}(rA_\phi). \end{aligned} \tag{25}$$

Under the self-similar assumption, the magnetic flux is conserved in both the $\hat{\phi}$ and $\hat{z}$ directions, i.e.,

$$\begin{cases} F_\phi = -l\int_0^R \frac{\partial A_z}{\partial r} dr = l(A_z(0) - A_z(R)) = \text{constant} \\ F_z = 2\pi\int_0^R \frac{\partial}{\partial r}(rA_\phi) dr = 2\pi R A_\phi(R) = \text{constant}. \end{cases}$$

In order to satisfy the self-similar expansion assumption, A_ϕ and A_z have to retain their own distributions. Therefore, A_ϕ and A_z can be expressed as

$$\begin{cases} A_\phi = f_{A\phi}(x)A_{\phi 0}(t) \\ A_z = f_{Az}(x)A_{z0}(t) \end{cases}.$$

Combining the above two sets of equations, we derive

$$\begin{cases} A_\phi(t, x) = \frac{f_{A\phi}(x)}{R} \\ A_z(t, x) = \frac{f_{Az}(x)}{l} \end{cases}. \tag{26}$$

Also, it can be proved that the total magnetic helicity (H_m) is conserved, and therefore, we can write

$$\begin{aligned} H_m &= \int \boldsymbol{B}.\boldsymbol{A} r dr d\phi dz \\ &= 2\pi\int_0^1 \left[f_{Az}\frac{\partial}{\partial x}(xf_{A\phi}) - xf_{A\phi}\frac{\partial f_{Az}}{\partial x}\right] dx = \text{constant}. \end{aligned} \tag{27}$$

Combining Equations (25) and (26), we can calculate the Lorentz force in the flux rope as

$$\begin{aligned}\boldsymbol{j}\times\boldsymbol{B} &= \frac{1}{\mu_0}(\nabla\times\boldsymbol{B})\times\boldsymbol{B}\\ &= -\frac{1}{\mu_0}\left\{\frac{1}{R^5 x}\frac{\partial}{\partial x}\left[\frac{1}{x}\frac{\partial}{\partial x}(xf_{A\phi})\right]\frac{\partial}{\partial x}(xf_{A\phi})\right.\\ &\quad\left.+\frac{1}{l^2R^3x}\frac{\partial}{\partial x}\left(x\frac{\partial f_{Az}}{\partial x}\right)\frac{\partial f_{Az}}{\partial x}\right\}\hat{\boldsymbol{r}}\\ \Rightarrow \overline{f}_{\rm em} &= \frac{2}{R^2}\int_0^R(\boldsymbol{j}\times\boldsymbol{B})_r r dr\\ &= -\frac{k_5}{\mu_0 R^5}-\frac{k_6}{\mu_0 l^2 R^3},\end{aligned} \tag{28}$$

where $k_5 = 2\int_0^1 \frac{\partial}{\partial x}\left[\frac{1}{x}\frac{\partial}{\partial x}(xf_{A\phi})\right]\frac{\partial}{\partial x}(xf_{A\phi})dx$ and $k_6 = 2\int_0^1 \frac{\partial}{\partial x}\left(x\frac{\partial f_{Az}}{\partial x}\right)\frac{\partial f_{Az}}{\partial x}dx \geqslant 0$ are both integral constants. The sign of k_5 is determined by $B_z^2(R) - B_z^2(0)$.

2.1.5. Governing Equation of Motion Relating the Measurable Parameters of the Flux Rope

From the observations of the present era, it is difficult to precisely measure the axial length (l) of a flux rope. However, it can be assumed that the axial length of the flux rope has a relationship with the distance (L) between the axis of the flux rope and the solar surface (Figure 1). L can be measured using imaging observations of the CME/flux rope, and therefore, we can write

$$l = k_7 L, \tag{29}$$

where k_7 is a positive constant. The combination of Equations (23), (28), and (29) results in the final equation

$$a_e - c_1 R^{-3} = c_2 L R^{-3} + c_3 L^{-1} R^{-1} + \lambda L^{1-\gamma} R^{1-\gamma}, \tag{30}$$

where the coefficients c_1–c_3 are constants, and λ is a time-dependent variable. They are given as

$$\begin{cases} c_1 = \dfrac{k_1^2 k_3 L_A^2}{k_2 M^2} \geqslant 0\\ c_2 = \dfrac{-k_5 k_7}{\mu_0 k_2 M}\\ c_3 = \dfrac{-k_6}{\mu_0 k_2 k_7 M} \leqslant 0\end{cases}, \tag{31}$$

$$\lambda(t) = c_0 e^{\sigma s(t)}, \tag{32}$$

where the coefficient c_0 is a constant, and $c_0 = \frac{k_4 M^{\gamma-1}}{k_2 k_7^{\gamma-1}}$. The left-hand side of Equation (30) describes the motion of the plasma in the flux rope. Its first and second terms give the acceleration due to the radial motion (i.e., the expansion or contraction) and the acceleration due to the poloidal motion, respectively. On the right-hand side of Equation (30), the first two terms represent the contribution from the Lorentz force, and the third term represents the contribution from the thermal pressure force. The expansion acceleration (a_e), distance between the axis of the flux rope and solar surface (L), and radius of the flux rope (R) in Equation (30) can be measured from the observations of the flux-rope CME. Thus, the unknown coefficients c_1–c_3 can be obtained by fitting the equation to the measurements as long as we have an additional constraint for the variable λ, which will be continued in Section 2.3.

2.2. Physical Parameters of the Internal State of CME

2.2.1. Lorentz, Thermal, and Centrifugal Forces

The average Lorentz force ($\overline{f}_{\rm em}$) and thermal pressure force ($\overline{f}_{\rm th}$) can be expressed by substituting the value of l from Equation (29) into Equations (28) and (24), respectively. Thus,

$$\overline{f}_{\rm em} = \frac{k_2 M}{k_7}(c_2 R^{-5} + c_3 L^{-2} R^{-3}), \tag{33}$$

$$\overline{f}_{\rm th} = \frac{k_2 M}{k_7}(\lambda L^{-\gamma} R^{-\gamma-1}). \tag{34}$$

The ratio between the average Lorentz force ($\overline{f}_{\rm em}$) and thermal pressure force ($\overline{f}_{\rm th}$) can be expressed as

$$\frac{\overline{f}_{\rm em}}{\overline{f}_{\rm th}} = \frac{c_2 L^{\gamma} R^{\gamma-4} + c_3 L^{\gamma-2} R^{\gamma-2}}{\lambda}.$$

Further, the poloidal motion should be maintained by an inward centripetal force, which is part of the sum of the Lorentz force and the thermal pressure gradient force. Therefore, the expression of the average outward centrifugal force ($\overline{f}_p$) due to the poloidal motion can be derived using the second term on the left-hand side of Equation (30) as

$$\overline{f}_p = \frac{k_2 M}{k_7}(c_1 R^{-5} L^{-1}). \tag{35}$$

2.2.2. Density, Temperature, and Thermal Pressure

Combining Equations (10) and (29), the average proton mass density ($\overline{\rho}$) and proton number density ($\overline{n}_p$) can be expressed as

$$\overline{\rho} = \frac{M}{k_7 \pi}(LR^2)^{-1}, \tag{36}$$

$$\overline{n}_p = \frac{M}{k_7 \pi m_p}(LR^2)^{-1}. \tag{37}$$

The average thermal pressure is given as

$$\begin{aligned}\overline{p}(t) &= \frac{2}{R^2}\int_0^R p r dr\\ &= \frac{k_2 k_8 M}{k_4 k_7}\lambda(LR^2)^{-\gamma},\end{aligned} \tag{38}$$

where $k_8 = \frac{2}{\pi^{\gamma}}\int_0^1 f_{\rho}^{\gamma} x dx > 0$ is a constant, and the average temperature ($\overline{T}(t)$) is given as

$$\begin{aligned}\overline{T}(t) &= \frac{m_p}{2k}\frac{\overline{p}}{\overline{\rho}}\\ &= \frac{\pi\sigma k_2 k_8}{(\gamma-1)k_4}\lambda(LR^2)^{1-\gamma}.\end{aligned} \tag{39}$$

2.2.3. Polytropic Index

The polytropic process can describe multiple expansion and compression processes which include heat transfer. The evolution of the polytropic index can be obtained from the

combination of Equations (22) and (32) as follows:

$$\lambda = c_0 b \rho^{\Gamma-\gamma}$$
$$\Gamma = \gamma + \frac{\ln\lambda - \ln(c_0 b)}{\ln\rho}. \quad (40)$$

Assume the thermodynamic process is quasi-static between each of two measurement points within a relatively short period, i.e., between the instants t and $t + \Delta t$. This implies that the values of Γ and b in Equation (40) are nearly constant during that time interval. Then, Equation (40) can be solved as

$$\begin{cases} \Gamma(t) = \gamma + \dfrac{\ln\lambda(t) - \ln(c_0 b(t))}{\ln\rho(t)} \\ \Gamma(t) \approx \gamma + \dfrac{\ln\lambda(t+\Delta t) - \ln(c_0 b(t))}{\ln\rho(t+\Delta t)} \end{cases}$$
$$\Rightarrow \Gamma(t) \approx \gamma + \frac{\ln\frac{\lambda(t)}{\lambda(t+\Delta t)}}{\ln\frac{\rho(t)}{\rho(t+\Delta t)}}$$
$$= \gamma + \frac{\ln\frac{\lambda(t)}{\lambda(t+\Delta t)}}{\ln\left\{\frac{L(t+\Delta t)}{L(t)}\left[\frac{R(t+\Delta t)}{R(t)}\right]^2\right\}}. \quad (41)$$

2.2.4. Rate of Change of Entropy and Heating Rate

Further, we derive the expression for the rate of change of entropy ($\frac{ds}{dt}$) per unit mass from the expression of λ as in Equation (32),

$$\frac{d\lambda}{dt} = \sigma\lambda\frac{ds}{dt}$$
$$\frac{ds}{dt} = \frac{1}{\sigma\lambda}\frac{d\lambda}{dt}. \quad (42)$$

Now, using the second law of thermodynamics as in Equation (18), we derive the expression for the average heating rate ($\overline{\kappa}$) per unit mass. This is given as

$$\overline{\kappa}(t) = \frac{dQ(t)}{dt} = \overline{T}\frac{ds}{dt}$$
$$= \frac{\pi k_2 k_8}{(\gamma-1)k_4}(LR^2)^{1-\gamma}\frac{d\lambda}{dt}. \quad (43)$$

2.2.5. Total Energies of the CME Plasma

The total thermal energy (E_i) and total magnetic energy (E_m) of the plasma associated with the flux-rope CME can be given as

$$E_i = 2\pi l\int_0^R \frac{p}{\gamma-1} r dr$$
$$= \frac{\pi k_2 k_8 M}{(\gamma-1)k_4}\lambda(LR^2)^{1-\gamma}, \quad (44)$$

$$E_m = 2\pi l\int_0^R \frac{B^2}{2\mu_0} r dr$$
$$= \frac{\pi k_9}{\mu_0 k_7}L^{-1} + \frac{\pi k_7 k_{10}}{\mu_0}LR^{-2}, \quad (45)$$

where $k_9 = \int_0^1 x\left(\frac{\partial f_{Az}}{\partial x}\right)^2 dx \geqslant 0$ and $k_{10} = \int_0^1 \frac{1}{x}\left[\frac{\partial}{\partial x}(x f_{A\phi})\right]^2 dx \geqslant 0$ are both integral constants.

2.3. Additional Constraint for the Derivation of the Unknown Coefficients and the Variable

The governing equation of motion for the expanding flux-rope CME as given in Equation (30) can be expressed as

$$\lambda = L^{\gamma-1}R^{\gamma-1}(a_e - c_1 R^{-3} - c_2 LR^{-3} - c_3 L^{-1}R^{-1}). \quad (46)$$

From Equation (46), we can write

$$\frac{d\lambda}{dt} = L^{\gamma-1}R^{\gamma-1}\Bigg[\left\{\frac{da_e}{dt} + (\gamma-1)(a_e v_e R^{-1} + a_e v_c L^{-1})\right\}$$
$$+ c_1\{(4-\gamma)v_e R^{-4} + (1-\gamma)v_c L^{-1}R^{-3}\}$$
$$+ c_2\{(4-\gamma)v_e LR^{-4} - \gamma v_c R^{-3}\}$$
$$+ c_3\{(2-\gamma)(v_e L^{-1}R^{-2} + v_c L^{-2}R^{-1})\}\Bigg]. \quad (47)$$

In Equation (46), R, L, and a_e are all of the known parameters that can be obtained from the measurements using coronagraphic observations of the CMEs, and the others are unknown parameters. However, Equation (46) only is not sufficient to obtain the unknown coefficients c_1–c_3 and the variable λ. Therefore, we need an additional constraint on λ to determine the unknown coefficients. For this purpose, we assume that irrespective of any heating mechanism in the CMEs, the heating rate ($\overline{\kappa}$) per unit mass of the CME plasma may be equivalently expressed as the result of heat flow. Thus,

$$\overline{\kappa} = k_{11}\frac{T_a - \overline{T}}{\overline{\rho}L^2}, \quad (48)$$

where k_{11} is an unknown positive constant, and T_a could be treated as the equivalent temperature of the ambient solar wind around the CME base, which serves as a heat source for the CME plasma. Equation (48) is analogous to the expression of heat flow per unit mass, $\frac{1}{\rho}\nabla\cdot\boldsymbol{q}$, in which $\boldsymbol{q}$ is the heat flux for conduction and proportional to ∇T. Substituting $\overline{\rho}$, $\overline{T}$, and $\overline{\kappa}$ in Equation (48) from those in Equations (36), (39), and (43), we get

$$(LR^2)^{\gamma-1} = c_4 LR^{-1}\frac{d\lambda}{dt} + c_5\lambda, \quad (49)$$

where the coefficients c_4 and c_5 are constants, which are given as

$$\begin{cases} c_4 = \dfrac{k_2 k_8 M}{(\gamma-1)k_4 k_7 k_{11} T_a} \\ c_5 = \dfrac{\pi\sigma k_2 k_8}{(\gamma-1)k_4 T_a} \end{cases}. \quad (50)$$

From the value of c_4, we can write the expression for the temperature (T_a) of the ambient solar wind around the CME base as

$$T_a = \frac{\pi\sigma k_2 k_8}{(\gamma-1)k_4 c_5}. \quad (51)$$

Substituting the value of λ and $d\lambda/dt$ from Equations (46) and (47) into Equation (49), we can finally write

$$\begin{aligned}(LR^2)^{\gamma-1} = L^{\gamma-1}R^{\gamma-1}[&c_5a_e + \{(\gamma-1)c_4a_ev_c \\ &- c_3c_5L^{-1} + c_4\frac{da_e}{dt}L\Big\}R^{-1} \\ &+ \{(2-\gamma)c_3c_4v_cL^{-1} + (\gamma-1)c_4a_ev_eL\}R^{-2} \\ &+ \{(2-\gamma)c_3c_4v_e - c_2c_5L - c_1c_5\}R^{-3} \\ &+ \{(1-\gamma)c_1c_4v_c - \gamma c_2c_4v_cL\}R^{-4} \\ &+ \{(4-\gamma)c_1c_4v_eL + (4-\gamma)c_2c_4v_eL^2\}R^{-5}],\end{aligned} \tag{52}$$

where v_c, v_e, a_e and da_e/dt are the propagation speed, expansion speed, expansion acceleration, and rate of change of the expansion acceleration of the flux rope, respectively. Now, the unknown constants c_1–c_5 serve as fitting parameters that can be obtained by fitting Equation (52) to the measurements of distance between the axis of the flux rope and the solar surface (L), the radius of the flux rope (R), and their derivatives. Once the constants are known, then the variable λ can be calculated from Equation (46). Further, the goodness of fit can be evaluated by the relative error in the quantity kept on the left-hand side of Equation (52), i.e., $(LR^2)^{\gamma-1}$.

If the flux-rope CME is evolving in such a way that its aspect ratio (R/L) is constant, then we can express $R = k_{12}L$, where k_{12} is a positive constant. It implies that the angular width of the flux rope or CME will not change during its heliospheric propagation. Consequently, the distance of the leading edge of the flux rope (h) is therefore given by $h = (1 + \frac{1}{k_{12}})R = (1 + k_{12})L$, and the speed and acceleration of the leading edge are $v_h = (1 + \frac{1}{k_{12}})v_e = (1 + k_{12})v_c$ and $a_h = (1 + \frac{1}{k_{12}})a_e = (1 + k_{12})a_c$, respectively. Therefore, for the flux rope having a constant aspect ratio, Equation (52) can be expressed as Equation (53), where h is used instead of R or L, because it is easier to measure h from the imaging observations of the CMEs:

$$\begin{aligned}&\left(\frac{k_{12}}{1+k_{12}}\right)^{\gamma+1}h^{\gamma} = \left[\left(\frac{k_{12}}{1+k_{12}}\right)^{3}\left(c_5a_h + \frac{c_4}{k_{12}}\frac{da_h}{dt}\right)\right]h \\ &- \left[c_5\left(\frac{c_2}{k_{12}} + c_3k_{12}\right)\right]h^{-1} - \left[c_1c_5\left(\frac{1+k_{12}}{k_{12}}\right)\right. \\ &\left. + 2(\gamma-2)\frac{c_4}{k_{12}}\left(\frac{c_2}{k_{12}} + c_3k_{12}\right)v_h\right]h^{-2} \\ &+\left[(5-2\gamma)c_1\frac{c_4}{k_{12}}\left(\frac{1+k_{12}}{k_{12}}\right)v_h\right]h^{-3}.\end{aligned} \tag{53}$$

Further, we know that for a force-free flux rope, $\boldsymbol{j} \times \boldsymbol{B} = 0$. Therefore, Equations (28) and (31) imply that the constants $k_5 = k_6 = 0$ and $c_2 = c_3 = 0$. Thus, Equations (52) and (53) can further be simplified under the constraint of a force-free flux-rope CME. However, for the present study, we use the general form of the formulations as expressed in Equation (52) to fit the kinematic data, which is explained in Section 3.2. Up to now, we have obtained all of the internal dynamic and thermodynamic parameters that could be derived by our FRIS model. The summary of the derived physical parameters and the constants are given in Table 1.

3. Application of the Model to the CME of 2008 December 12

3.1. Observations and Measurements from Coronagraphs

The CME is well observed by *SOHO*/LASCO and the Sun–Earth Connection Coronal and Heliospheric Investigation (SECCHI; Howard et al. 2008) coronagraphs and the Heliospheric Imagers (HIs) on board *STEREO*. This CME was observed in SECCHI/COR1-A images at 04:35 UT in the NE quadrant and in SECCHI/COR1-B at 04:55 UT in the NW quadrant. *SOHO*/LASCO observed this CME as a partial halo with an angular width of 184° and a linear speed of 203 km s^{-1}. This CME was tracked in LASCO-C3 images out to 12 $R_\odot$ where its quadratic speed was measured as 322 km s^{-1}. The CME was associated with a prominence eruption that started at 03:00 UT in the NE quadrant observed in SECCHI/EUVI-A 304 Å images. Prominences are always above polarity inversion lines and believed to be supported by a surrounding coronal magnetic field, which may develop into a flux rope and therefore a CME when an eruption takes place (Demoulin & Priest 1989; Martens & van Ballegooijen 1990; Gibson & Fan 2006; Okamoto et al. 2008; Vemareddy et al. 2017). Thus, the orientation of a prominence usually indicates the axis of the CME flux rope. According to this picture, the CME was approximately viewed on axis in *STEREO-A* and viewed from the side in *STEREO-B*. We tracked the CME from the inner corona to the outer corona and noted that it took about 11 hr for the leading edge to travel from 1.4 to 15 $R_\odot$, which implies its slow speed.

As has been described in Section 2.1, we treat a CME as a flux rope, and the input parameters of our model are the radius (R) of the cross-section of the CMEs, the distance (L) between the axis of the flux rope and the solar surface, and their derivatives. There are various approaches to obtain R and L for a CME. In earlier studies of Wang et al. (2009), the R and L for the 2009 October 8 CME is derived by measuring the heliocentric distance (h) of the leading edge of that CME as well as its span angle ($\Delta\theta$). Such an approach is suitable for CMEs having unambiguous boundaries and viewed along the axis. The front of the 2008 December 12 CME studied here is diffusive (or fainter), and it is difficult to precisely measure its leading edge and span angle, although it did have an axial view in *STEREO-A*. Therefore, we used the graduated cylindrical shell (GCS) model (Thernisien et al. 2009; Thernisien 2011) to recover the three-dimensional geometry (including R and L) of the CME from the projected images of the CME. The GCS forward modeling method has been frequently used to determine the 3D kinematics of the flux-rope CMEs (Lynch et al. 2010; Gui et al. 2011; Bosman et al. 2012; Vourlidas et al. 2013; Wang et al. 2014, 2018; Mishra et al. 2015, 2016).

The model has nine free parameters (refer to Table 1 of Thernisien et al. 2006), in which six parameters determine the CME shape projected on the plane of the sky. These parameters, called geometric parameters, are the longitude (ϕ), latitude (θ), height (or heliocentric distance) of the leading edge (h), aspect ratio (a), tilt angle, and half angle between the two legs of the flux rope. As per our experience of using the GCS model, a set of reasonable initial values of the free parameters is crucial for the model to get the correct values of

Table 1
List of the Derived Internal Thermodynamic Parameters, Constants, and Coefficients from the FRIS Model

Internal Thermodynamic Parameters Derived from the Model			
Quantities	Factors	Values	SI Units
Lorentz force ($\overline{f}_{\rm em}$)	$\frac{k_2M}{k_7}$	$c_2R^{-5}+c_3L^{-2}R^{-3}$	Pa m^{-1}
Thermal pressure force ($\overline{f}_{\rm th}$)	$\frac{k_2M}{k_7}$	$\lambda L^{-\gamma}R^{-\gamma-1}$	Pa m^{-1}
Centrifugal force ($\overline{f}_p$)	$\frac{k_2M}{k_7}$	$c_1R^{-5}L^{-1}$	Pa m^{-1}
Proton number Density ($\overline{n}_p$)	$\frac{M}{k_7}$	$\frac{1}{\pi m_p}(LR^2)^{-1}$	kg m^{-3}
Thermal pressure ($\overline{p}$)	$\frac{k_2k_8M}{k_4k_7}$	$\lambda(LR^2)^{-\gamma}$	Pa
Temperature ($\overline{T}$)	$\frac{k_2k_8}{k_4}$	$\frac{\pi\sigma}{\gamma-1}\lambda(LR^2)^{1-\gamma}$	K
Changing rate of entropy ($\frac{ds}{dt}$)		$\frac{1}{\sigma\lambda}\frac{d\lambda}{dt}$	J K^{-1} kg^{-1} s^{-1}
Heating rate ($\overline{\kappa}$)	$\frac{k_2k_8}{k_4}$	$\frac{\pi}{\gamma-1}(LR^2)^{1-\gamma}\frac{d\lambda}{dt}$	J kg^{-1} s^{-1}
Thermal energy (E_i)	$\frac{k_2k_8M}{k_4}$	$\frac{\pi}{\gamma-1}\lambda(LR^2)^{1-\gamma}$	J
Magnetic energy (E_m)		$E_{m1}+E_{m2}$	J
E_{m1}	$\frac{k_9}{k_7}$	$\frac{\pi}{\mu_0}L^{-1}$	J
E_{m2}	k_7k_{10}	$\frac{\pi}{\mu_0}LR^{-2}$	J
Polytropic index (Γ)		$\gamma+\frac{\ln\frac{\lambda(t)}{\lambda(t+\Delta t)}}{\ln\left\{\frac{L(t+\Delta t)}{L(t)}\left[\frac{R(t+\Delta t)}{R(t)}\right]^2\right\}}$	

All of the Constants (k_{1-12}) Introduced in the Model	
Constants	Interpretations
k_1	Scale of the magnitude of the poloidal motion
$k_2-k_6,\ k_8-k_{10}$	Integrals of the distributions of density, poloidal speed, and magnetic vector potential
k_7	Ratio of the length of the flux rope l to the distance L
k_{11}	Coefficient of equivalent conductivity
k_{12}	Aspect ratio, i.e., the ratio of the radius of the flux rope R to the distance L

All of the Coefficients (c_{0-5}) Introduced in the Model	
Coefficients	Expressions
c_0	$\frac{k_4M^{\gamma-1}}{k_2k_7^{\gamma-1}}$
c_1	$\frac{k_1^2k_3L_A^2}{k_2M^2}\geqslant 0$
c_2	$\frac{-k_5k_7}{\mu_0k_2M}$
c_3	$\frac{-k_6}{\mu_0k_2k_7M}\leqslant 0$
c_4	$\frac{k_2k_8M}{(\gamma-1)k_4k_7k_{11}T_a}$
c_5	$\frac{\pi\sigma k_2k_8}{(\gamma-1)k_4T_a}$

Note. Top panel: quantity = factor × value. The factors are unknown constants that cannot be inferred from the FRIS model. The distance (L) of the center of the flux-rope CME from the solar surface and its radius (R) can be derived from the observations. The variable λ is given by Equation (49). γ is the heat capacity ratio (adiabatic index), and μ_0 is the magnetic permeability of free space. $\sigma=\frac{(\gamma-1)m_p}{2k}$, where m_p is the proton mass and k is the Boltzmann constant. M is the total mass of a CME. Middle panel: among the constants, $k_{2,7,8,11}>0$ and $k_{3,6,9,10}\geqslant 0$. Bottom panel: the coefficients (c_{0-5}) are also constants and can be derived from the model. L_A is the total angular momentum of a flux-rope CME, and T_a is the equivalent temperature of the ambient solar wind around the CME base.

the parameters, except that we manually adjust the initial values to make the modeled flux rope match the CME's 2D projected geometry as much as possible. We also used observations of the source region of the CME to constrain the tilt angle of the flux rope, as the tilt angle should be roughly aligned with the polarity inversion line associated with the CME.

We applied the GCS forward-fitting model to the contemporaneous images of the CMEs obtained from the SECCHI/COR2-B, *SOHO*/LASCO-C3, and SECCHI/COR2-A coronagraphs as shown in the images overlaid with the fitted GCS wireframed contour (Figure 2). The obtained longitude, latitude, tilt angle, aspect ratio, and half angle are 6°.7, 10°.6, −15° (i.e., clockwise from the ecliptic plane), 0°.29, and 15°, respectively, at the height of 11.4 $R_\odot$. The 2008 December 12 CME has been studied earlier by several researchers using *STEREO* COR and HI observations as well as MHD simulations (Davis et al. 2009; Byrne et al. 2010; Liu et al. 2010a, 2010b; Poomvises et al. 2010; Gui et al. 2011; Mishra & Srivastava 2013). Based on the tracking of different features of this CME in HI observations, Davis et al. (2009) estimated the propagation direction of the CME to be at maximum −15° to 15° away from the Sun–Earth line. In another study, using the GCS model, Liu et al. (2010a) showed that the CME has a propagation direction of about 10° west of the Sun–Earth line and 8° above the ecliptic plane, with a tilt angle of about −53° clockwise from the ecliptic plane. The CME is found to show a deflection as it propagated away from the Sun and a physical explanation of this has been addressed in Gui et al. (2011). The GCS fitted parameters in Poomvises et al. (2010) are within a 10% uncertainty of those estimated in the present study, except for the tilt angle and aspect ratio of the CME, which are found to be 87° and 0.10, respectively, in their study. Using the tie-pointing method of 3D reconstruction (Inhester 2006; Thompson 2009) on the COR data, Mishra & Srivastava (2013) estimated the longitude and latitude of the CME as 5° at 15 $R_\odot$. Thus, in the present study, the values of the fitted parameters for the CMEs, except for the tilt angle, which usually has a large uncertainty, are in fair agreement with those estimated in earlier studies. For the purpose of using the FRIS model, the radius (R) and the distance (L) are derived from the precise measurement of the height (h) and aspect ratio (a) of the flux rope. The radius of the flux rope is given by $R=\frac{a}{1+a}h$, and its distance as $L=h-R-1\,R_\odot$. We also defined the heliocentric distance of the CME center as $D=L+1\,R_\odot$.

We tracked the CME from $D=2$ to 14 $R_\odot$, and during this interval its radius expanded to about 4 $R_\odot$, the propagation speed slowly accelerated to about 350 km s^{-1}, the expansion speed reached to about 100 km s^{-1}, and both the propagation and expansion accelerations were positive with peaks at about $D=2.5\,R_\odot$. The CME showed an impulsive expansion acceleration and then a deceleration phase in the COR1 field of view (FOV), which continued up to the COR2 FOV, and then again a slight increase in the accelerations is observed. Since our FRIS model assumes that the CME/flux rope is undergoing a self-similar expansion, it is not surprising that the model would not be suitable for deriving the internal parameters of the CME near the Sun in the COR1 FOV. This issue be discussed further in Sections 3.2 and 4. Therefore, we have applied the FRIS model to the measurements of the CME derived from the COR2 observations alone. Figure 3 presents the time variation of the heliocentric distance (D), radius (R),

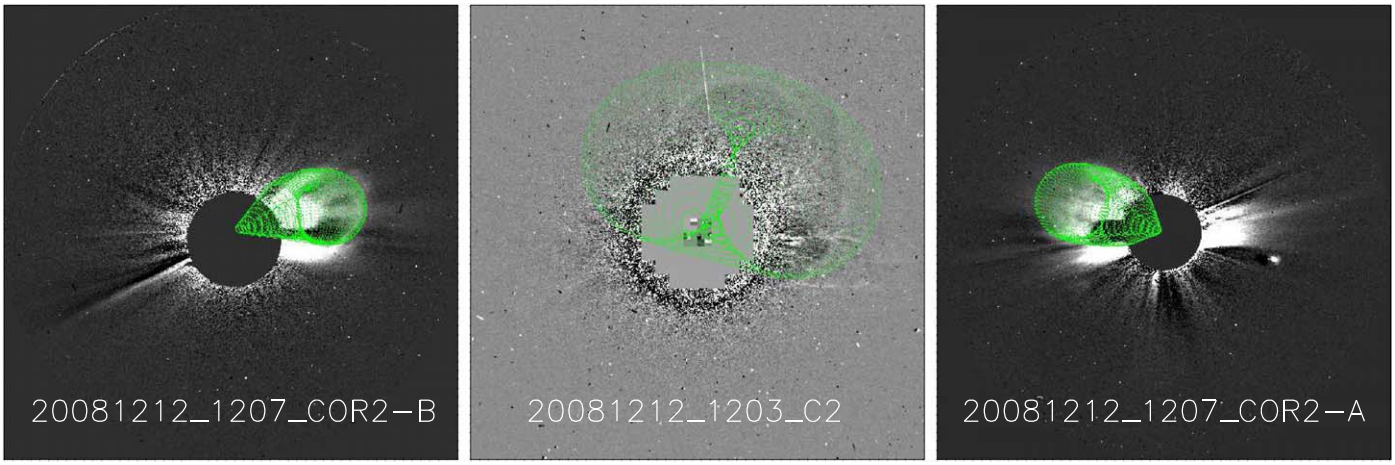

Figure 2. GCS model wireframe in green is overlaid on the images of the 2008 December 12 CME. The triplet of concurrent images are taken from *STEREO*/COR2-B (left), *SOHO*/LASCO-C2 (middle), and *STEREO*/COR2-A (right) around 12:07 UT on 2008 December 12.

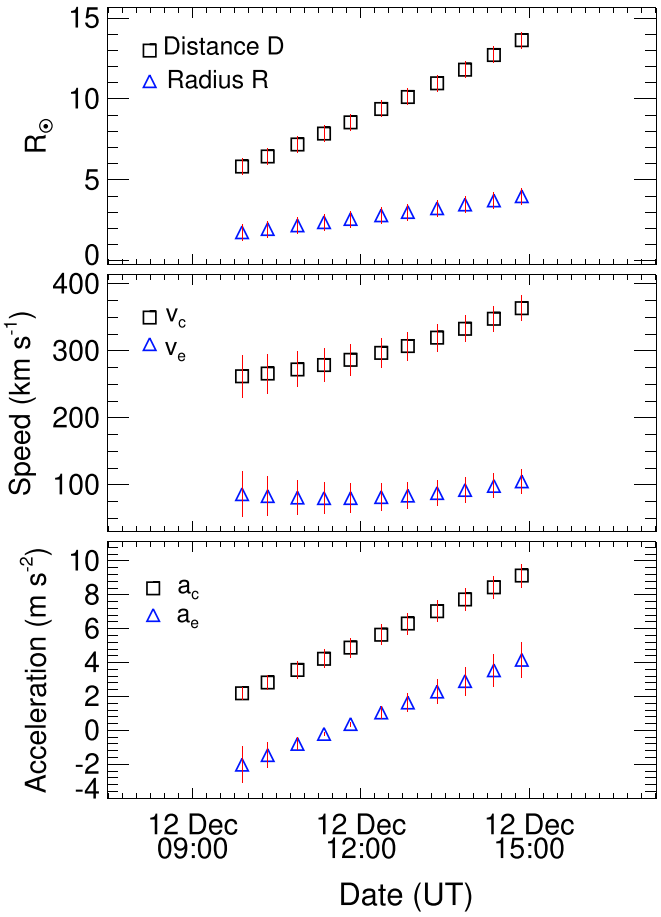

Figure 3. Top panel: the measurements of the heliocentric distance (D) of the center of flux rope associated with the CME and its radius (R). Middle panel: the propagation speed (v_c) and expansion speed (v_e) derived by taking the derivatives of D and R, respectively. Bottom panel: the propagation acceleration (a_c) and expansion acceleration (a_e) derived by taking the derivative of v_c and v_e, respectively. The vertical lines at each data point show the error bars derived by arbitrarily assuming an error of 0.5 $R_\odot$ in the measurements of D and R from coronagraph observations.

propagation speed (v_c), expansion speed (v_e), propagation acceleration (a_c), and expansion acceleration (a_e) of the CME of 2008 December 12 observed in the COR2 FOV.

3.2. Internal Thermodynamic Parameters of the CME

The obtained kinematic parameters shown in Figure 3 are used as inputs to the FRIS model. We fit Equation (52) and determine the value of unknowns in the equation. Thus, we fit the general equation and do not use its simplistic form for a force-free flux rope, which governs the motion of the CME as conceptualized in the FRIS model. For this purpose, first, the parameter $(LR^2)^{\gamma-1}$ kept in the left-hand side of Equation (52) is determined directly from the measured data of the CME. Then, we fit the measured results of $(LR^2)^{\gamma-1}$ with the model-derived expression as in the right-hand side of Equation (52) to find the best set of unknown model fitting parameters (i.e., c_1–c_5) which match the measured results in a least-squares sense. The fitting was performed using the MPFITFUN routine of IDL, which can fit a user-supplied model to a set of user-supplied measured data (Markwardt 2009). Second, we input the obtained values of c_1–c_5 and observed kinematic parameters in Equations (46) and (47) and determine the value of λ and $d\lambda/dt$, respectively. Finally, once the values of λ, its derivative, and c_1–c_5 are known, we can estimate several internal thermodynamic parameters of the CME.

Performing the fitting as explained above, the goodness of fit is shown in Figure 4. In the figure, the plus symbols represent the quantity $(LR^2)^{\gamma-1}$, defined as Q_m, directly derived from the measurements. The thick blue line represents the model result, defined as Q_f, from the right-hand side of Equation (49). The uncertainty in the model results is estimated from the relative error as given by

$$E = \left| \frac{Q_m - Q_f}{Q_m} \right|. \tag{54}$$

The relative error is indicated by the connected triangles in red and plotted on right y-axis in Figure 4. In the plot, the values of R, L, and D are kept in units of $R_\odot$, and value of $\gamma = 5/3$ is set. The model result matches very well with the measurements. The relative errors of all the points are below 1% when the CME is in the COR2 FOV. We mention here that we have also attempted to fit the model to the measurements in the COR1 FOV and found that the relative error reached more than 10% indicating a poor fitting. This is another reason, in addition to the violation of self-similar expansion in the COR1 FOV, to avoid inclusion of the analysis when the CME is in the COR1 FOV. It has also been pointed out in Paper I that

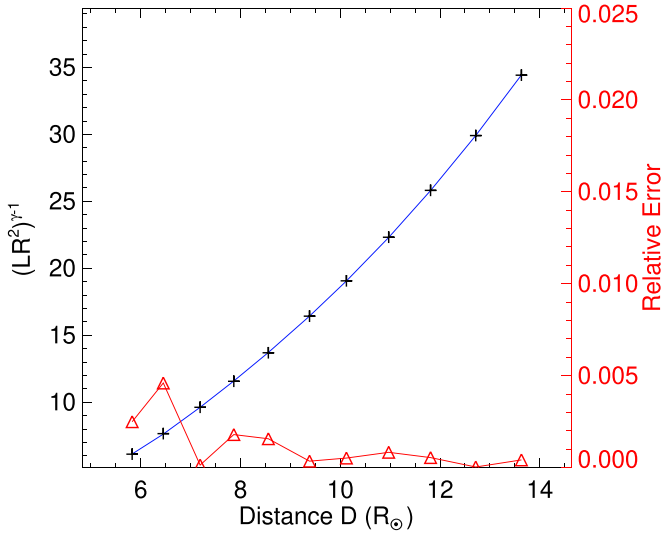

Figure 4. The profile of $(LR^2)^{\gamma-1}$ from the measurements (black), the modeled result for this parameter (blue), and the relative error (red) are shown.

ignoring the gravitational force and the equivalent fictitious force due to the use of a non-inertial reference frame of the Sun may cause a lager error in the FRIS model at the near-Sun region. Therefore, in the next section, we present the internal properties of the CME only in the COR2 FOV.

3.3. Thermodynamic Process

3.3.1. Polytropic Index, Density, Temperature, and Thermal Pressure

We used Equations (37)–(39) and (41) to estimate the average proton number density ($\overline{n}_p$), thermal pressure ($\overline{p}$), temperature ($\overline{T}$), and polytropic index (Γ). The estimated parameters are shown in Figure 5. It is noted that except for Γ, other parameters are given in a relative value because of the unknown factors. From the top-left panel of the figure, it is found that Γ is decreasing as the CME is evolving through the corona. Near the Sun, when the center of the CME is at a heliocentric distance of $D = 5.8\,R_\odot$, the value of the polytropic index is about 1.8. Its value is decreasing slowly and reaches around 1.66 at $9\,R_\odot$. The value of $\Gamma > 1.66$ means that the CME is releasing heat into its surroundings. Thus, we are not considering the CME as an isolated system. After $D = 9\,R_\odot$, Γ showed a faster decrease and went down to about 1.37, meaning that the CME is absorbing heat. It is also to be noted that although the propagation speed of the CME always increased, the expansion speed first decreased up to around $9\,R_\odot$ and then began increasing (Figure 3).

CMEs are usually hot plasma structures originating from active regions mostly through magnetic field reconnection. Thus, initially, CMEs have a temperature higher than that of the ambient solar wind (Antonucci et al. 1997; Ciaravella et al. 2000) and deliver heat to its surroundings. The expansion of the CME leads to some work done by it and causes the temperature decrease (as shown in the bottom-left panel of Figure 5). According to our model results, before $D = 9\,R_\odot$, the expansion has not been sufficient, and therefore, the value of Γ is greater than 1.66.

The continuous expanding propagation of the CME leads to a decrease of its density (top-right panel of Figure 5), which in addition to a decrease in temperature (bottom-left panel of the figure) results in a decrease in thermal pressure (bottom-right panel of the figure) inside the CME. At the beginning, the decrease in proton density, temperature, and thermal pressure is much faster and then becomes slower, tending toward its asymptotic values. The exact physical mechanisms responsible for the transfer of heat as energy need to be explored further. It is possible that heat is conducted from the lower corona to the CME as the looped structure of a CME is considered to be always attached to the Sun (Gosling et al. 1987; Larson et al. 1997). As the temperature of the ambient solar wind is higher than that in the CME in the outer corona, the ambient medium can be an additional source to heat the CME. However, the cross-field diffusion of particles is more limited than the motion parallel to magnetic field lines (Matthaeus et al. 2003; Qin et al. 2006; Ruffolo et al. 2008).

3.3.2. Heat and Entropy

The rate of change of entropy (i.e., $ds/dt = \overline{\kappa}/\overline{T}$) per unit mass and average heating rate (i.e., $\overline{\kappa} = dQ/dt$) per unit mass is estimated using Equations (42) and (43). The estimated value of ds/dt is shown in the top-left panel of Figure 6. The value of ds/dt derived by the model is absolute, unlike that of other parameters (e.g., density, temperature, heat etc.), of which only the relative values are known. The plot of ds/dt is very useful as the heating rate per mass of the CME plasma can be read from it if the real temperature were known. The value of ds/dt was about $-0.75\ \mathrm{J\,kg^{-1}\,K^{-1}\,s^{-1}}$ at the beginning and reached zero at about $D = 9\,R_\odot$ and continuously increased to about $0.8\ \mathrm{J\,kg^{-1}\,K^{-1}\,s^{-1}}$ at $D = 13.6\,R_\odot$. It implies that the rate of loss of entropy was getting smaller as the CME moved out and then after $D = 9\,R_\odot$, the CME started to gain entropy with increasing rate. It is also clear from the top-right panel of the figure that the added entropy (ds) is negative in the beginning, i.e., the release of entropy is taking place from the CME. Then, the ds increased toward positive values, implying a transfer of entropy into the CME system.

The bottom-left panel of Figure 6 shows that the value of the heating rate $\overline{\kappa} = dQ/dt$ was negative at the beginning and increased toward positive values after crossing zero at $D = 9\,R_\odot$. Negative values of $\overline{\kappa}$ imply that the CME is releasing heat, while positive values imply that the CME is absorbing heat. The heat absorbed (dQ) by the CME is elegantly shown in the bottom-right panel of the figure. The positive values of dQ imply that thermal energy is being transferred from somewhere into the CME while its negative values mean that thermal energy is being released by the CME. We note that the CME behaves like an adiabatic closed system at $D = 9\,R_\odot$, where the change in entropy is zero, and this suggests that no entropy is generated within the system boundaries.

3.4. Dynamic Process

3.4.1. Lorentz, Thermal, and Centrifugal Forces

The dynamic processes that could be deduced by our FRIS model are the changes of the average Lorentz force ($\overline{f}_{\mathrm{em}}$), thermal pressure force ($\overline{f}_{\mathrm{th}}$), and centrifugal force ($\overline{f}_p$) as the CME propagated away from the Sun, and these are shown in Figure 7. From the top panel of the figure, it is noted that $\overline{f}_{\mathrm{em}}$ have negative values whereas there are positive values for the $\overline{f}_{\mathrm{th}}$. Thus, the directions of the two forces are opposite, which indicate that $\overline{f}_{\mathrm{em}}$ is acting toward the center of the CME and $\overline{f}_{\mathrm{th}}$ is acting away from the center of the CME. The force directions

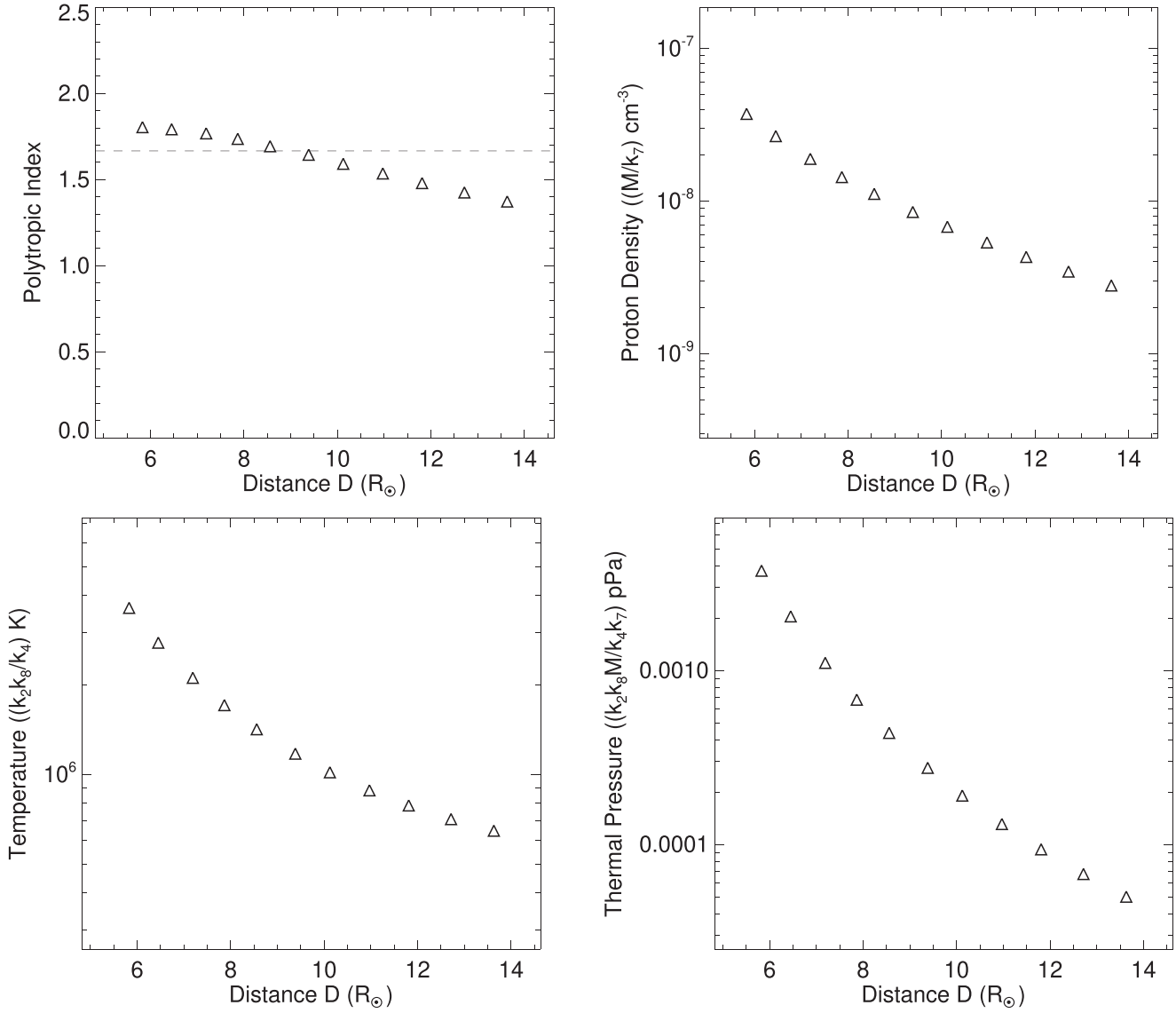

Figure 5. Variation of the polytropic index (Γ), average proton number density ($\overline{n_p}$), temperature ($\overline{T}$), and thermal pressure ($\overline{p}$) of the CME with the heliocentric distance of the CME's center (D) is shown in the top-left, top-right, bottom-left, and bottom-right panels, respectively.

suggest that (1) $\overline{f}_{\rm em}$ prevented the CME from freely expanding and also maintained a possible poloidal motion of the CME plasma, and (2) $\overline{f}_{\rm th}$ was the internal cause of the CME expansion. The bottom-left panel of the figure shows that $\overline{f}_p$ drops quickly with around an 85% decrease before the center of the CME reaches $8\,R_\odot$, and the decrease continues further, asymptotically reaching zero.

The expansion acceleration of the flux-rope plasma is driven by the Lorentz force + thermal pressure gradient force—centripetal force, which is what Equation (23) describes (i.e., the net force $\overline{f} = \overline{f}_{\rm em} + \overline{f}_{\rm th} + \overline{f}_p$). The centripetal force is part of the sum of the Lorentz force and thermal pressure gradient force. Thus, the poloidal motion has nothing to do with the expansion acceleration. The net force ($\overline{f}$) inside the CME and the ratio of the average Lorentz to thermal forces ($\overline{f}_{\rm em}/\overline{f}_{\rm th}$) is shown in the bottom-right panel of Figure 7. It is evident that the absolute values of both the $\overline{f}_{\rm em}$ and $\overline{f}_{\rm th}$ forces get very close to each other as the CME moves outward. The ratio of the two forces indicates that $\overline{f}_{\rm em}$ is stronger than $\overline{f}_{\rm th}$ since the beginning of $10\,R_\odot$, where they become almost the same in the magnitude. After this distance, $\overline{f}_{\rm th}$ becomes larger in magnitude than $\overline{f}_{\rm em}$. Thus, the ratio of their absolute values range between 1.33 at the beginning and 0.74 at the last data point. The net force inside the CME is negative at the first four data points, and this is expected as the expansion acceleration is less than zero (i.e., negative), corresponding to these points as shown in Figure 3. Starting from $D = 8.5\,R_\odot$ to $13.6\,R_\odot$, the net force is positive, corresponding to the positive expansion acceleration of the CME.

We note that there are three data points between around 8.5 and $10\,R_\odot$ where the expansion acceleration is positive despite having a larger inward $\overline{f}_{\rm em}$ than $\overline{f}_{\rm th}$. Thus, the poloidal motion in the CME tends to contribute to the expansion, and its presence suggests that flux ropes carry some angular momentum. Such an angular momentum may be generated locally through the interaction with the ambient solar wind through viscosity (Wang et al. 2015; Zhao et al. 2017b, 2017a). Although there is no direct evidence for plasma rotation inside a CME near the Sun, the rotation signature is indeed found in in situ measurements of magnetic clouds at 1 au (Wang et al. 2015,

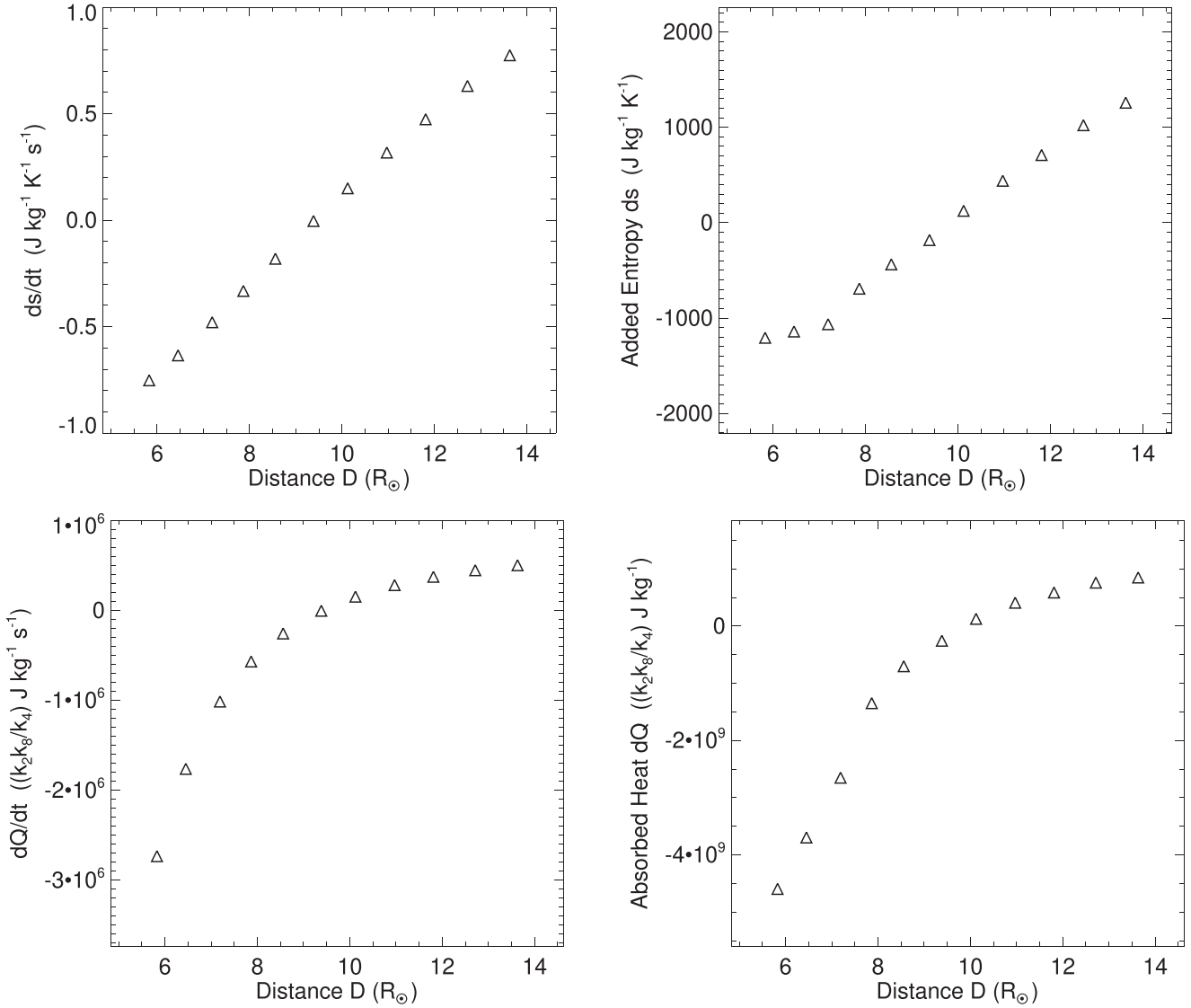

Figure 6. Variation of the rate of change of entropy (ds/dt) of the CME, added entropy (s) to the CME, heating rate ($\overline{\kappa} = dQ/dt$) of the CME, and absorbed heat (Q) with the heliocentric distance of the CME's center (D) is shown in the top-left, top-right, bottom-left, and bottom-right panels, respectively.

2016; Zhao et al. 2017a, 2017b). Based on a statistical study, it was found in Wang et al. (2015) that the poloidal motion is not as significant as the expanding motion generally. They noted that the median value of the poloidal speed was about 10 km s^{-1} at 1 au, while for a few cases, the modeled poloidal speed was two to four times larger than the modeled expansion speed. Therefore, it was suggested that poloidal motion may also be recognized in observations. Further verification from observations is needed to confirm the presence of such poloidal motion inside a CME near the Sun.

4. Summary and Discussion

In the present study, we have improved the analytical FRIS model for investigating the evolution of the internal thermodynamic state of a CME. The model is constrained by the observed propagation and expansion behavior of a CME. The internal thermodynamic parameters derived from the model and the details of the constants introduced in the model are summarized in Table 1. We have applied the FRIS model to the CME of 2008 December 12 and determined the evolution of its internal properties. We find that the polytropic index of the CME plasma decreased from initially 1.8 to 1.66 slowly and then quickly decreased down to around 1.35. It suggests that initially there was heat released by the CME before reaching an adiabatic state, and then a continuous injection of heat into the CME plasma. The value of the polytropic index obtained in our study is not in good agreement with that obtained in Liu et al. (2005, 2006) using combined surveys of ICMEs in in situ observations. However, their estimated polytropic index of 1.1–1.3 was for the distance between 0.3 and 20 au while the CME we have studied was within 15 solar radii from the Sun.

We also find that the Lorentz force is directed inward while the thermal pressure force and centrifugal force are directed outward from the center of the CME. All three forces decreased as the CME propagated away from the Sun. The time variation of the resultant direction of the net force is consistent with the expansion acceleration, which reveals that the thermal pressure force is the internal driver of CME expansion, whereas the Lorentz force prevented the CME from expanding. We emphasize that, in general, the direction of the Lorentz force may be either inward or outward, i.e., the Lorentz force can

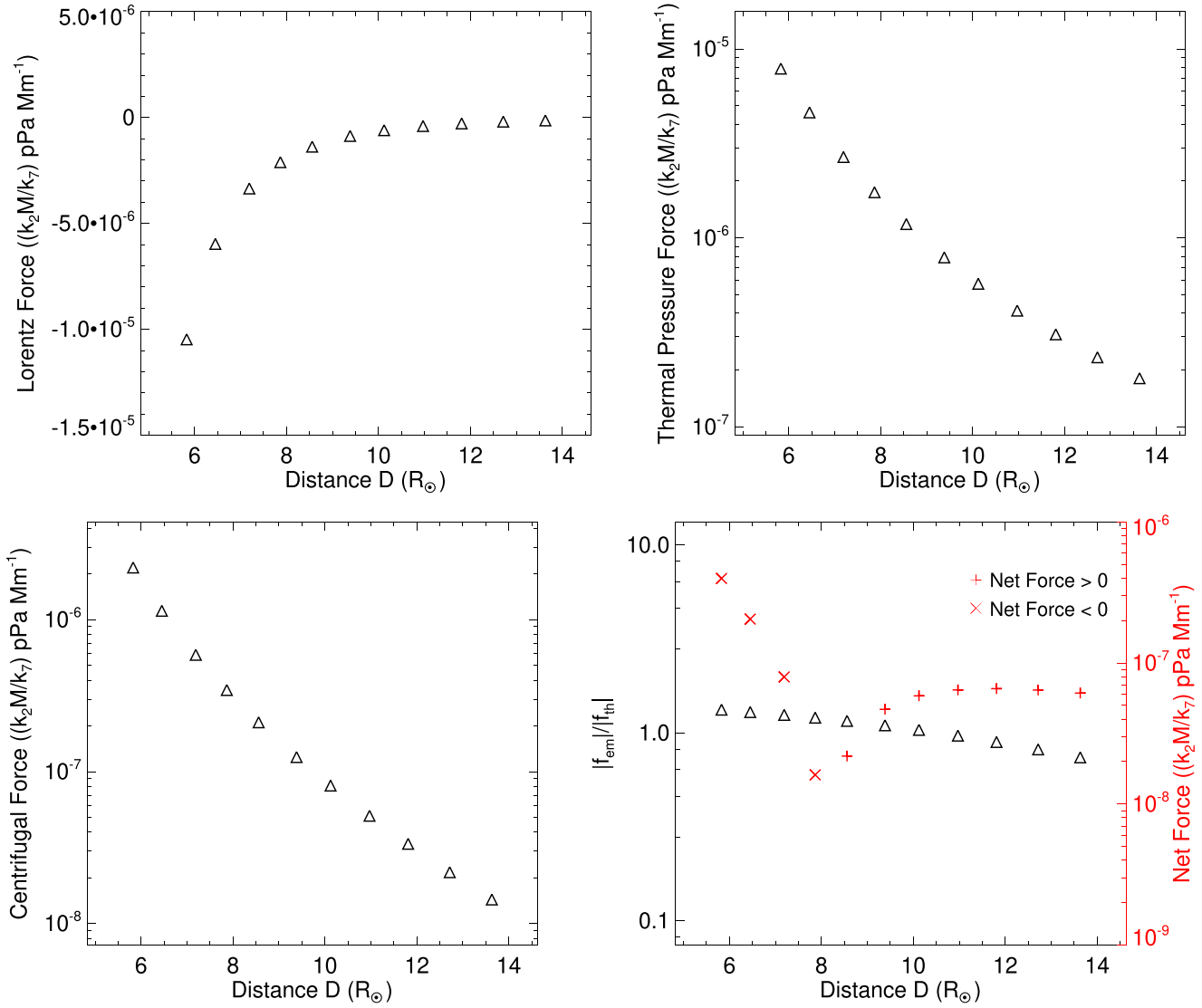

Figure 7. Variation of different forces acting on the CME with the heliocentric distance of its center (D) is shown. The average Lorentz force ($\overline{f}_{em}$), thermal pressure force ($\overline{f}_{th}$), and centrifugal force ($\overline{f}_p$) are shown in the top-left, top-right, and bottom-left panels, respectively. The ratio of the absolute values of the Lorentz and thermal forces (on the left Y-axis) as well as the net force (on right Y-axis) acting inside the CME ($\overline{f}$) is shown in the bottom-right panel.

cause both expansion and contraction of the flux rope. As is obvious from Equation (28), the constant k_6 is always larger than or equal to zero, while the sign of the constant k_5 is determined by $B_z^2(R)$–$B_z^2(0)$. It implies that $J_\phi \times B_z$ could contribute to contraction or expansion depending on the distribution of B_z in the cross-section of the flux rope. Also, it can be noted from Equation (33) that the direction of the Lorentz force depends on the unknowns c_2 and c_3. The coefficient c_3 is always less than or equal to zero while the sign of the coefficient c_2 depends on the constant k_5. For the CME under study, on fitting Equation (52), the value of c_2 was estimated to be less than zero. This implies that the sign of k_5 was positive. Therefore, the direction of the Lorentz force was inward, which prevented the CME from expanding. Based on the obtained results, we note that the negative expansion acceleration, the Lorentz force dominating the thermal force, and the release of heat happen together. Moreover, we find that among the three forces, the centrifugal force decreased with the fastest rate and the Lorentz force decreased slightly faster than the thermal pressure force. We note that even a small difference between the Lorentz and thermal forces can drive the expansion acceleration of the CME at the order of 1 m s^{-2}.

As a consequence of the release and absorption of heat by the CME, a decrease in the entropy during the initial phase and an increase in the entropy at the latter phases of CME propagation are found. Our analysis found that the rate of heat release and entropy loss of the CME slowed down with time, gradually turning into an increasing rate of heat absorption and entropy gain. Thus, the CME studied here is found to go through an isentropic (adiabatic and reversible, no heat transfer) point around 9 $R_\odot$, after which the expansion acceleration of the CME is positive. Since heat is a disorganized form of energy, the direction of entropy transfer is the same as the direction of heat transfer.

This CME launched with a hot temperature from the lower corona of the Sun through a rapid magnetic energy release process and then cooled down during expansion. The heat released by the CME in its initial propagation phase before around 9 $R_\odot$ is probably due to the CME structure not having

expanded sufficiently and therefore still hotter than the ambient coronal medium. However, the CME is found to be heated in the latter phase of its propagation. The heating could be possibly due to the conduction of heat from the solar surface or solar wind, or due to the dissipation of magnetic energy into thermal energy (Liu et al. 2006). Kumar & Rust (1996) suggested that the heating may result from the local magnetic dissipation as they have shown that around 58% of the magnetic energy lost in the expansion is available for the heating.

In our study, we attempted to apply the FRIS model to the complete measurements from the COR1 and COR2 observations. However, we faced difficulty in fitting the governing Equation (49) for the CME measurements in the COR1 FOV, for which the model was not reliable. We think that the rising and declining phases of the CME acceleration in the COR1 FOV and then a gap in the measurements between the COR1 and COR2 FOVs could be the reasons for the unreliability. We also tried to separate the observations of the acceleration and deceleration phases, and then fit each phase with the model. This also could not improve the fitting as the number of data points was not sufficient enough. Based on these trials, we decided not to include the COR1 measurements in the present study. This is logical as the CME may not follow a self-similar expansion, which is one of the basic assumptions of the FRIS model, during its impulsive acceleration phase near the Sun. Moreover, gravitational forces and the equivalent fictitious force in a non-inertial frame are not considered in FRIS model. Although these forces are very small for most CMEs beyond the outer corona, they may, however, significantly distort the model results for some CMEs that have a slow expansion acceleration in the inner corona near the Sun.

Further, there have been studies on the solar wind stretching effect caused by the divergent radial expansion of solar wind flow, which is a kinematic effect, on the expansion of CMEs (Newkirk et al. 1981; Suess 1988; Crooker & Intriligator 1996; Riley et al. 2003; Riley & Crooker 2004). Due to this effect, a flux-rope CME in the solar wind does not remain in cylindrical shape but rather becomes a convex-outward, "pancake" shape. These studies confirm that the self-similar assumption is broken gradually as the CME moves away from the Sun. Earlier studies have suggested that the self-similar assumption is a valid approximation when the CME is nearly force-free and not too far away from the Sun (Low 1982; Burlaga 1988; Chen et al. 1997; Démoulin & Dasso 2009; Shapakidze et al. 2010; Subramanian et al. 2014). We expect that the FRIS model would be suitable to apply to CME observations from a couple of solar radii (i.e., the COR2 FOV) to within tens of solar radii from the Sun. In another study, we plan to estimate the internal parameters of the CME beyond the coronagraphic FOV using CME measurements from HI1 observations.

In the FRIS model, some effects of coupling between the ambient solar wind and the CMEs have been implicitly included. The drag interaction between the CMEs and the solar wind, causing momentum exchange between them, has an effect on the propagation speed (i.e., v_c) of the CMEs (Cargill 2004; Manoharan 2006; Vršnak et al. 2010; Subramanian et al. 2012; Mishra & Srivastava 2013; Liu et al. 2016). Further, the pressure in the ambient solar wind has the effect of preventing the free expansion (i.e., v_e) of CMEs (Dal Lago et al. 2003; Démoulin & Dasso 2009; Gulisano et al. 2010). These effects of the solar wind on a CME give rise to different time variations of L and R, which can be measured from imaging data, and therefore are included in the model. Moreover, the distortion of the circular cross-section of the flux rope is not considered, mainly because of the difficulty of the derivation of the model.

Following the discussion in Paper I, another limitation of the model is due to the assumption of an axisymmetric cylindrical flux rope, and thus the curvature of the axis of the flux rope is not considered in the model. The axial curvature causes the Lorentz force to have an additional component for driving the CME in the heliosphere. Ignoring the axial curvature generally would cause an underestimation of the Lorentz force from the model. We emphasize that the distortion of the circular cross-section of the flux rope would cause an overestimation of its radius (R) and an underestimation of its distance (L) from the solar surface. Therefore, it is expected that from our measurements, the expansion speed is overestimated and the propagation speed is underestimated. Thus we find that in our study, the density, thermal pressure force, and Lorentz force are more underestimated than its actual values. However, the extent of the underestimation would be different at different distances from the Sun. We expect that errors in the derived internal thermodynamic parameters would not be significant at smaller distances, i.e., within the COR2 FOV, where the distortion in the circular cross-section is not much.

The FRIS model described in this study is an improved version of the flux-rope model developed earlier in Paper I. In Paper I, the authors have made a comparison of their model with that of Kumar & Rust (1996), and the differences described there would also be valid for the improved version of the model. It would be interesting to extrapolate the estimated internal thermodynamic properties of the CMEs to far away from the Sun, up to around 1 au. This can be done by extrapolating the observed kinematics using a drag-based model (Vršnak et al. 2013) of CMEs or by directly measuring the kinematics from imaging observations. The uncertainty from the model can further be examined based on the CME measurements from in situ observations. In a separate study, we would focus on the quantification of errors due to the breakdown of some of the assumptions in the model. Further, it would be worth examining if other CMEs also show an evolution of their thermodynamic parameters similar to those of the 2008 December 12 CME studied here.

We acknowledge the UK Solar System Data Center (UKSSDC) for providing the *STEREO*/COR2 data. Y.W. is supported by the National Natural Science Foundation of China (NSFC) grant Nos. 41574165, 41774178, and 41761134088. W.M. is supported by NSFC grant No. 41750110481 and the Chinese Academy of Sciences (CAS) President's International Fellowship Initiative (PIFI) grant No. 2015PE015. W.M. thanks Ying D. Liu (CAS, China) for the helpful discussion.

ORCID iDs

Wageesh Mishra https://orcid.org/0000-0003-2740-2280
Yuming Wang https://orcid.org/0000-0002-8887-3919

References

Akmal, A., Raymond, J. C., Vourlidas, A., et al. 2001, ApJ, 553, 922
Antonucci, E., Kohl, J. L., Noci, G., et al. 1997, ApJL, 490, L183
Baker, D. N. 2009, SpWea, 7, 02003
Bemporad, A., & Mancuso, S. 2010, ApJ, 720, 130
Bosman, E., Bothmer, V., Nisticò, G., et al. 2012, SoPh, 281, 167

Burlaga, L., Sittler, E., Mariani, F., & Schwenn, R. 1981, JGR, 86, 6673
Burlaga, L. F. 1988, JGR, 93, 7217
Byrne, J. P., Maloney, S. A., McAteer, R. T. J., Refojo, J. M., & Gallagher, P. T. 2010, NatCo, 1, 74
Cargill, P. J. 2004, SoPh, 221, 135
Chen, J., Howard, R. A., Brueckner, G. E., et al. 1997, ApJL, 490, L191
Chen, P. F. 2011, LRSP, 8, 1
Ciaravella, A., Raymond, J. C., Thompson, B. J., et al. 2000, ApJ, 529, 575
Ciaravella, A., Raymond, J. C., van Ballegooijen, A., et al. 2003, ApJ, 597, 1118
Cliver, E. W., & Hudson, H. S. 2002, JASTP, 64, 231
Crooker, N. U., & Intriligator, D. S. 1996, JGR, 101, 24343
Dal Lago, A., Schwenn, R., & Gonzalez, W. D. 2003, AdSpR, 32, 2637
Davies, J. A., Harrison, R. A., Perry, C. H., et al. 2012, ApJ, 750, 23
Davis, C. J., Davies, J. A., Lockwood, M., et al. 2009, GeoRL, 36, 8102
DeForest, C. E., Howard, T. A., & McComas, D. J. 2013, ApJ, 769, 43
Démoulin, P., & Dasso, S. 2009, A&A, 498, 551
Demoulin, P., & Priest, E. R. 1989, A&A, 214, 360
Domingo, V., Fleck, B., & Poland, A. I. 1995, SoPh, 162, 1
Forsyth, R. J., Bothmer, V., Cid, C., et al. 2006, SSRv, 123, 383
Gibson, S. E., & Fan, Y. 2006, JGRA, 111, A12103
Goldstein, M. L., Roberts, D. A., & Matthaeus, W. H. 1995, ARA&A, 33, 283
Gopalswamy, N., Dal Lago, A., Yashiro, S., & Akiyama, S. 2009, CEAB, 33, 115
Gosling, J. T., Baker, D. N., Bame, S. J., et al. 1987, JGR, 92, 8519
Gui, B., Shen, C., Wang, Y., et al. 2011, SoPh, 271, 111
Gulisano, A. M., Démoulin, P., Dasso, S., Ruiz, M. E., & Marsch, E. 2010, A&A, 509, A39
Harrison, R. A., Davies, J. A., Barnes, D., et al. 2018, SoPh, 293, 77
Howard, R. A., Moses, J. D., Vourlidas, A., et al. 2008, SSRv, 136, 67
Howard, T. A., Fry, C. D., Johnston, J. C., & Webb, D. F. 2007, ApJ, 667, 610
Hundhausen, A. J., Sawyer, C. B., House, L., Illing, R. M. E., & Wagner, W. J. 1984, JGR, 89, 2639
Inhester, B. 2006, arXiv:astro-ph/0612649
Jian, L. K., Russell, C. T., Luhmann, J. G., Skoug, R. M., & Steinberg, J. T. 2008, SoPh, 250, 375
Kaiser, M. L., Kucera, T. A., Davila, J. M., et al. 2008, SSRv, 136, 5
Kilpua, E. K. J., Mierla, M., Rodriguez, L., et al. 2012, SoPh, 279, 477
Kohl, J. L., Noci, G., Cranmer, S. R., & Raymond, J. C. 2006, A&ARv, 13, 31
Kumar, A., & Rust, D. M. 1996, JGR, 101, 15667
Larson, D. E., Lin, R. P., McTiernan, J. M., et al. 1997, GeoRL, 24, 1911
Lee, J.-Y., Raymond, J., Ko, Y.-K., & Kim, K.-S. 2009, ApJ, 692, 1271
Lepri, S. T., Zurbuchen, T. H., Fisk, L. A., et al. 2001, JGR, 106, 29231
Liu, Y., Davies, J. A., Luhmann, J. G., et al. 2010b, ApJL, 710, L82
Liu, Y., Richardson, J. D., & Belcher, J. W. 2005, P&SS, 53, 3
Liu, Y., Richardson, J. D., Belcher, J. W., Kasper, J. C., & Elliott, H. A. 2006, JGRA, 111, A01102
Liu, Y., Thernisien, A., Luhmann, J. G., et al. 2010a, ApJ, 722, 1762
Liu, Y. D., Hu, H., Wang, C., et al. 2016, ApJS, 222, 23
Lopez, R. E., Goodrich, C., Wiltberger, M., & Lyon, J. 2000, JASTP, 62, 865
Low, B. C. 1982, ApJ, 254, 796
Low, B. C. 2001, JGR, 106, 25141
Lugaz, N., Vourlidas, A., & Roussev, I. I. 2009, AnGp, 27, 3479
Lynch, B. J., Li, Y., Thernisien, A. F. R., et al. 2010, JGRA, 115, 7106
Manchester, W. B., Gombosi, T. I., Roussev, I., et al. 2004, JGRA, 109, A02107
Manoharan, P. K. 2006, SoPh, 235, 345
Markwardt, C. B. 2009, in ASP Conf. Ser. 411, Astronomical Data Analysis Software and Systems XVIII, ed. D. A. Bohlender, D. Durand, & P. Dowler (San Francisco, CA: ASP), 251
Martens, P. C. H., & van Ballegooijen, A. A. 1990, GMS, 58, 337
Matthaeus, W. H., Qin, G., Bieber, J. W., & Zank, G. P. 2003, ApJL, 590, L53
Mishra, W., & Srivastava, N. 2013, ApJ, 772, 70
Mishra, W., & Srivastava, N. 2015, JSWSC, 5, A20
Mishra, W., Srivastava, N., & Singh, T. 2015, JGRA, 120, 10221
Mishra, W., Wang, Y., & Srivastava, N. 2016, ApJ, 831, 99
Mishra, W., Wang, Y., Srivastava, N., & Shen, C. 2017, ApJS, 232, 5
Munro, R. H., Gosling, J. T., Hildner, E., et al. 1979, SoPh, 61, 201
Newkirk, G., Jr., Hundhausen, A. J., & Pizzo, V. 1981, JGR, 86, 5387
Okamoto, T. J., Tsuneta, S., Lites, B. W., et al. 2008, ApJL, 673, L215
Poomvises, W., Zhang, J., & Olmedo, O. 2010, ApJL, 717, L159
Pulkkinen, T. 2007, LRSP, 4, 1
Qin, G., Matthaeus, W. H., & Bieber, J. W. 2006, ApJL, 640, L103
Raymond, J. C. 2002, in ESA Special Publication 508, From Solar Min to Max: Half a Solar Cycle with SOHO, ed. A. Wilson (Noordwijk: ESA Publications), 421
Richardson, I. G., & Cane, H. V. 1993, JGR, 98, 15295
Riley, P., & Crooker, N. U. 2004, ApJ, 600, 1035
Riley, P., Linker, J. A., Mikić, Z., et al. 2003, JGRA, 108, 1272
Rollett, T., Möstl, C., Isavnin, A., et al. 2016, ApJ, 824, 131
Ruffolo, D., Chuychai, P., Wongpan, P., et al. 2008, ApJ, 686, 1231
Schwenn, R. 2006, LRSP, 3, 2
Schwenn, R., dal Lago, A., Huttunen, E., & Gonzalez, W. D. 2005, AnGeo, 23, 1033
Shapakidze, D., Debosscher, A., Rogava, A., & Poedts, S. 2010, ApJ, 712, 565
Shen, C., Chi, Y., Wang, Y., Xu, M., & Wang, S. 2017, JGRA, 122, 5931
Subramanian, P., Arunbabu, K. P., Vourlidas, A., & Mauriya, A. 2014, ApJ, 790, 125
Subramanian, P., Lara, A., & Borgazzi, A. 2012, GeoRL, 39, 19107
Suess, S. T. 1988, JGR, 93, 5437
Thernisien, A. 2011, ApJS, 194, 33
Thernisien, A., Vourlidas, A., & Howard, R. A. 2009, SoPh, 256, 111
Thernisien, A. F. R., Howard, R. A., & Vourlidas, A. 2006, ApJ, 652, 763
Thompson, W. T. 2009, Icar, 200, 351
Totten, T. L., Freeman, J. W., & Arya, S. 1995, JGR, 100, 13
Tousey, R. 1973, in Space Research XIII, ed. M. Rycroft & S. Runcorn (Berlin: Akademie-Verlag), 713
Vemareddy, P., Gopalswamy, N., & Ravindra, B. 2017, ApJ, 850, 38
Vourlidas, A., Lynch, B. J., Howard, R. A., & Li, Y. 2013, SoPh, 284, 179
Vršnak, B., Žic, T., Falkenberg, T. V., et al. 2010, A&A, 512, A43
Vršnak, B., Žic, T., Vrbanec, D., et al. 2013, SoPh, 285, 295
Wang, C., Du, D., & Richardson, J. D. 2005, JGRA, 110, A10107
Wang, C., & Richardson, J. D. 2004, JGRA, 109, A06104
Wang, Y., Shen, C., Liu, R., et al. 2018, JGRA, 123, 3238
Wang, Y., Wang, B., Shen, C., Shen, F., & Lugaz, N. 2014, JGRA, 119, 5117
Wang, Y., Zhang, J., & Shen, C. 2009, JGRA, 114, A10104
Wang, Y., Zhou, Z., Shen, C., Liu, R., & Wang, S. 2015, JGRA, 120, 1543
Wang, Y., Zhuang, B., Hu, Q., et al. 2016, JGRA, 121, 9316
Wang, Y. M., Ye, P. Z., Wang, S., Zhou, G. P., & Wang, J. X. 2002, JGRA, 107, 1340
Webb, D. F., Cliver, E. W., Crooker, N. U., Cry, O. C. S., & Thompson, B. J. 2000, JGR, 105, 7491
Webb, D. F., & Howard, T. A. 2012, LRSP, 9, 3
Zhao, A., Wang, Y., Chi, Y., et al. 2017a, SoPh, 292, 58
Zhao, A., Wang, Y., Liu, J., et al. 2017b, ApJ, 845, 109
Zurbuchen, T. H., Fisk, L. A., Lepri, S. T., & von Steiger, R. 2003, in AIP Conf. Ser. 679, Solar Wind Ten, ed. M. Velli et al. (Melville, NY: AIP), 604